Geophys. J. Int. (2003) **153,** 609–626

Assessment of crustal velocity models using seismic refraction and reflection tomography

Colin A. Zelt,[1] Kalachand Sain,[2] Julia V. Naumenko[1,*] and Dale S. Sawyer[1]

[1]*Department of Earth Science, Rice University, Houston,* TX 77005-1892, *USA. E-mail: czelt@rice.edu*
[2]*National Geophysical Research Institute, Hyderabad* 500 007, *India*

Accepted 2002 December 12. Received 2002 November 11; in original form 2002 June 6

Downloaded from https://academic.oup.com/gji/article/153/3/609/671989 by U.S. Department of Justice user on 16 August 2022

SUMMARY

Two tomographic methods for assessing velocity models obtained from wide-angle seismic traveltime data are presented through four case studies. The modelling/inversion of wide-angle traveltimes usually involves some aspects that are quite subjective. For example: (1) identifying and including later phases that are often difficult to pick within the seismic coda, (2) assigning specific layers to arrivals, (3) incorporating pre-conceived structure not specifically required by the data and (4) selecting a model parametrization. These steps are applied to maximize model constraint and minimize model non-uniqueness. However, these steps may cause the overall approach to appear ad hoc, and thereby diminish the credibility of the final model. The effect of these subjective choices can largely be addressed by estimating the minimum model structure required by the least subjective portion of the wide-angle data set: the first-arrival times. For data sets with Moho reflections, the tomographic velocity model can be used to invert the P_mP times for a minimum-structure Moho. In this way, crustal velocity and Moho models can be obtained that require the least amount of subjective input, and the model structure that is required by the wide-angle data with a high degree of certainty can be differentiated from structure that is merely consistent with the data. The tomographic models are not intended to supersede the preferred models, since the latter model is typically better resolved and more interpretable. This form of tomographic assessment is intended to lend credibility to model features common to the tomographic and preferred models. Four case studies are presented in which a preferred model was derived using one or more of the subjective steps described above. This was followed by conventional first-arrival and reflection traveltime tomography using a finely gridded model parametrization to derive smooth, minimum-structure models. The case studies are from the SE Canadian Cordillera across the Rocky Mountain Trench, central India across the Narmada-Son lineament, the Iberia margin across the Galicia Bank, and the central Chilean margin across the Valparaiso Basin and a subducting seamount. These case studies span the range of modern wide-angle experiments and data sets in terms of shot–receiver spacing, marine and land acquisition, lateral heterogeneity of the study area, and availability of wide-angle reflections and coincident near-vertical reflection data. The results are surprising given the amount of structure in the smooth, tomographically derived models that is consistent with the more subjectively derived models. The results show that exploiting the complementary nature of the subjective and tomographic approaches is an effective strategy for the analysis of wide-angle traveltime data.

Key words: inversion, seismic modelling, seismic refraction, seismic tomography, traveltime, wide-angle reflection.

1 INTRODUCTION

Velocity models obtained from wide-angle seismic traveltime data can be interpreted in terms of the composition and physical state of the subsurface, often in conjunction with other geological or geophysical data. In addition, velocity models can provide structural information in the form of layer thickness and depth variations, either from the models themselves or by facilitating the depth conversion of coincident multichannel seismic (MCS) reflection data. However, the constraint on velocity and interface structure provided by

*Now at: SeismicCity, Inc., Houston, TX 77042, USA.

© 2003 RAS

wide-angle traveltimes is inherently limited, even for data acquired using closely spaced source and receiver arrays (Zelt 1999). This is mainly because the subsurface is inadequately sampled by the waves that propagate between the surface source and receiver points, although wave front healing and the utilization of only a small portion of each seismogram (the traveltimes) are also factors. This means there is usually a significant amount of model non-uniqueness so that a range of models can adequately satisfy the wide-angle traveltime data.

A number of subjective steps are often taken to reduce the non-uniqueness and increase the model constraint. For example, two common steps that may be considered quite subjective include dividing a model into multiple layers and assigning refracted and reflected arrivals to individual layers, and automated forward modelling, in which the model is 'steered' in a direction considered geologically reasonable over several iterations. This is in contrast to a 'pure' tomographic approach in which a smooth model is sought using only first-arrival times and a uniform fine-grid model parametrization (e.g. Lees & Crosson 1989; Scales *et al.* 1990; Zelt & Barton 1998). In addition, pure tomography usually involves fitting the data in a series of linearized iterations without manual intervention, starting with a simple starting model. Using only the first-arrival times means that the picks do not have to be classified, other then that they should be the earliest event on the seismograms; picking a later event, such as a reflection, even a prominent one, is inherently more subjective, given that its onset may be buried within the coda.

In comparison, the medical imaging problem does not suffer from the same degree of non-uniqueness as the seismic problem since the source and detector arrangement can be optimally configured around the perimeter of the object to be imaged. Within the seismic realm, the wide-angle inversion problem is more non-linear than other problems (e.g. crosswell and global) since the raypaths, in addition to the velocity model, are poorly known at the outset. In practical terms, non-linearity means that one cannot be sure that the best model (i.e. global minimum) has been found. Thus, the three factors that most strongly characterize the wide-angle traveltime problem are non-uniqueness, non-linearity and the subjective steps taken to minimize the non-uniqueness and deal with the non-linearity. Taken together, these factors can create a significant problem in terms of the credibility of the preferred final model.

This credibility problem led us to ask the following question: what if the most objective inverse approach possible that uses the least subjective portion of the wide-angle data set yields a model that contains the same or similar features as in the preferred model, particularly those features that are important to the geological interpretation? If this were true, it would be the ideal case one could hope for in terms of defending a particular model. This paper presents an objective approach for estimating the minimum model structure required by the least subjective portion of the wide-angle data set: the traveltimes of the first-arrivals, and what is typically the most prominent reflection event, P_mP (Moho reflections). Using this approach, model structure that is required by the wide-angle data with a high degree of certainty can be differentiated from structure that is only required by the more uncertain and subjective elements of the modelling/inversion procedure. The more objective models, derived by refraction and reflection tomography, are not intended to supersede the preferred model, since the subjective steps normally result in a better resolved model that is more interpretable and more inline with pre-conceived geological notions. Instead, the tomographic approach is intended to lend credibility to those model features that are similar in the preferred and tomographic models. We call this approach 'tomographic assessment'.

To demonstrate the effectiveness of tomographic assessment, we have chosen four case studies that span the range of modern crustal wide-angle experiments and data sets in terms of shot–receiver spacing, marine and land acquisition, lateral heterogeneity of the study area, and the availability of wide-angle reflections and coincident MCS data. The four study areas are the Canadian Cordillera of southeastern British Columbia (Zelt & White 1995; Clowes *et al.* 1995), the Narmada-Son lineament of central India (Sain *et al.* 2000), the Galicia portion of the Iberia passive margin (Zelt *et al.* 2003) and the convergent margin of central Chile across the Valparaiso Basin near the subducting Juan Fernández ridge (von Huene *et al.* 1997; Flueh *et al.* 1998; Zelt *et al.* 1999; Naumenko 2001) (Fig. 1). In each case, a preferred model was derived first using one or more of the subjective steps described in the next section, followed by tomographic assessment.

This paper focuses on the tomographic assessment of each preferred model; only those details of how the preferred models were obtained that are necessary to place the comparisons in context are presented. By demonstrating the effectiveness of tomographic assessment, this paper also addresses several related issues, such as the robustness of refraction and reflection tomography, how the more subjective modelling steps provide the 'sharpness' in the preferred models, guidelines for 'interpreting' smooth tomographic models, and survey design. This paper serves as a companion to Zelt (1999) by presenting real case studies using the two end-member modelling/inversion styles advocated by Zelt (1999).

2 WIDE-ANGLE TRAVELTIME MODELLING AND INVERSION

When modelling or inverting wide-angle traveltime data for 2-D crustal velocity and interface structure, common steps that may be viewed as being subjective or ad hoc include: (1) the use of later refracted and reflected arrivals, particularly when they are difficult to pick within the seismic coda, (2) the assignment of refracted and reflected arrivals to specific model layers within or from which the corresponding raypaths bottom or reflect, (3) the use of sparely parametrized models comprised of irregularly distributed velocity and interface nodes, (4) the incorporation of features into the starting model based on prior information or what is considered geologically reasonable, (5) honouring prior information throughout the modelling, not just in constructing the starting model, (6) the incorporation of features into the starting and/or final model based on amplitudes of the wide-angle phases and (7) the application of only one algorithm and approach to derive and assess the final model.

Using later arrivals provides an additional model constraint, but classifying these picks with respect to type and model layer, as required by most algorithms, is subject to error, including the misidentification of multiples, conversions, diffractions and out-of-plane events. Also, classifying a set of phases the same way from multiple-shot or receiver gathers that actually represent more than one phase will probably introduce large errors. Later arrivals are almost always more difficult to pick since they occur within the seismic coda. For refracted first-arrivals it is possible to: (1) pre-assign specific model layers within which the corresponding raypaths bottom, (2) calculate times for each layer and choose the raypath yielding the fastest time (Zelt 1999) or (3) use a smooth model without layers and only calculate the first-arriving raypaths and times. The first approach is more subjective and subject to error, particularly since changes in apparent velocity may be due to lateral variations in the Earth. However, pre-assignment has the advantage of yielding a layered model

Downloaded from https://academic.oup.com/gji/article/153/3/609/671989 by U.S. Department of Justice user on 16 August 2022

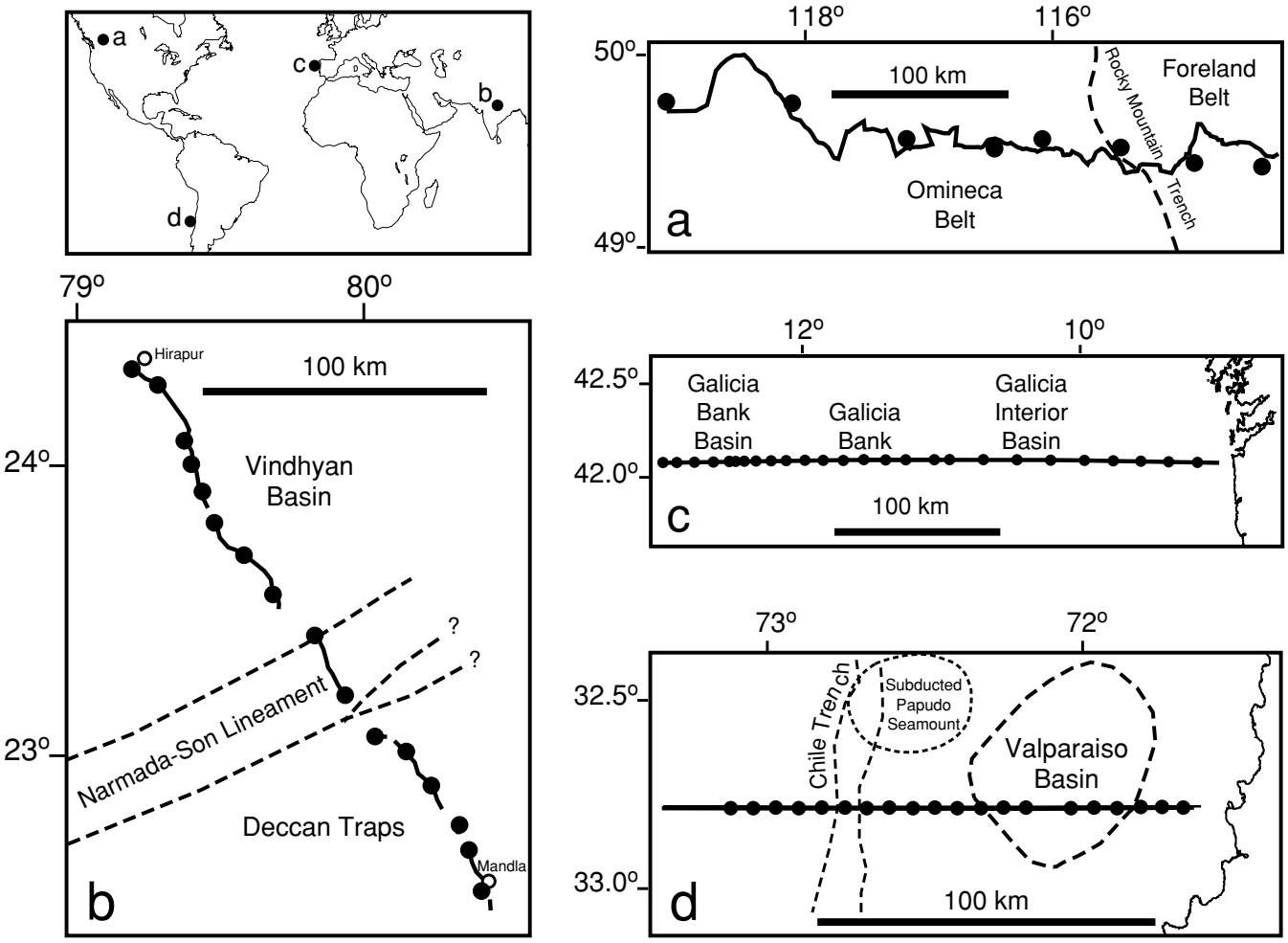

Figure 1. Survey geometries and major geological features. (a) Southeastern Canadian Cordillera across the Omineca and Foreland belts and the Rocky Mountain Trench; (b) central India across the Narmada-Son lineament, Deccan Traps and the Vindhyan Basin; (c) Iberia margin across the Galicia Interior Basin, Galicia Bank and Galicia Bank Basin where the *S* reflector is observed; (d) Chilean margin across the Valparaiso forearc basin and near the subducted Papudo seamount. The solid dots and thick lines for the land surveys indicate the shot locations and receiver arrays; the solid dots and thick lines for the marine surveys indicate the ocean-bottom receiver locations and airgun profiles. Location of each study area is indicated in the world map.

that will probably be easier to interpret geologically. In the second approach the layers may represent nothing more than a modelling convenience to allow changes in velocity gradient.

Using a non-uniform, sparsely parametrized model (e.g. Zelt & Smith 1992) makes it relatively easy to incorporate model features based on prior information and to maintain these features as much as possible during iterative forward or inverse modelling. The disadvantages of sparely parametrized models include the bias introduced by the parametrization, as well as the possibility of restricting model resolution. More importantly, there will be a greater potential for including model structure that is consistent with, but not required by, the traveltimes. The main reason for using prior information is to reduce the degree of model non-uniqueness; if the observed data can uniquely determine all model parameters, there is no need for prior information. A concern when using prior information is that it may be wrong or inappropriate, and thus lead to unnecessary or incorrect model structure. One particular form of prior information that is often used comes from amplitude modelling of wide-angle data (e.g. Zelt & White 1995). Given that amplitudes are sensitive to small-scale structure that cannot be resolved by either traveltime or amplitude data (Levander & Holliger 1992), the wisdom of using amplitudes, except to constrain very large-scale structure, is questionable. Our approach to tomographic assessment is to use as little prior information as possible and seek the minimum-structure model that satisfies the data.

This paper compares the results of applying two different inverse methods to the same set of wide-angle traveltime data. Since every forward and inverse modelling approach makes some assumptions to make the problem solvable, it is significant when two approaches that make very different assumptions yield the same solution. The few real data examples where a second approach has been applied to the same data have yielded important insights into the behaviour of the methods and the nature of the constraint supplied by the data (e.g. White & Boland 1992; Zelt 1994; Zelt & Barton 1998; Lutter *et al.* 1999; Korenaga *et al.* 2000).

3 DATA AND PREFERRED MODELS

3.1 Southeastern British Columbia

The wide-angle data from southeastern British Columbia were acquired in 1990 as part of the Lithoprobe programme (Clowes *et al.*

Downloaded from https://academic.oup.com/gji/article/153/3/609/671989 by U.S. Department of Justice user on 16 August 2022

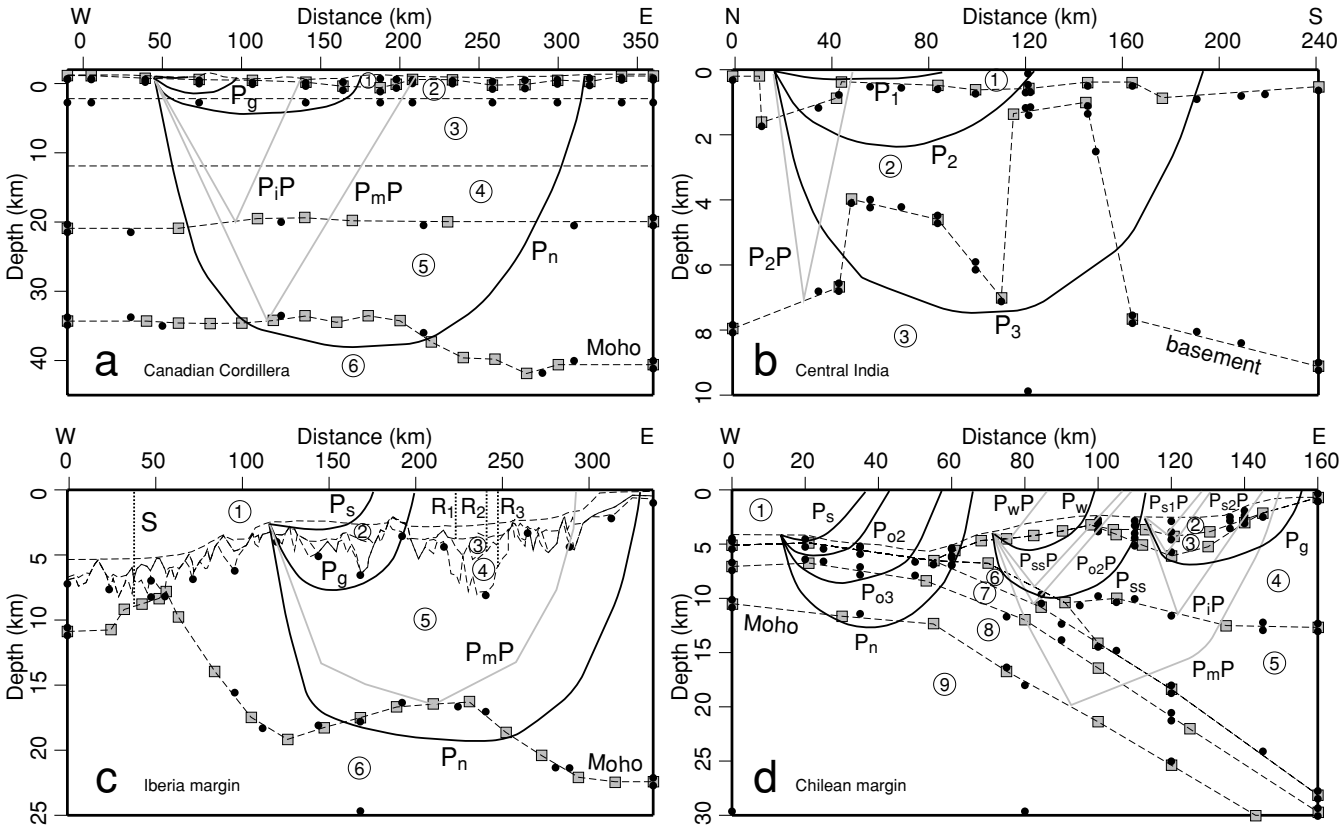

Figure 2. Model parametrizations and phases for the preferred models. (a) Southeastern Canadian Cordillera; (b) central India; (c) Iberia margin; (d) Chilean margin. Dashed lines are layer boundaries, dots are velocity nodes, squares are boundary nodes. Schematic raypath for each type of phase used to derive the preferred model is indicated and labelled: black lines are refracted rays, grey lines are reflected rays, and dotted lines in (c) are reflected rays for the coincident MCS data. Layer numbers are circled. The Moho boundary is labelled in each case, except in (b) where the basement is labelled.

1995; Zelt & White 1995). The 350 km-long east–west profile crosses the Rocky Mountain Trench separating the two easternmost orogen-parallel morphogeological belts of the Canadian Cordillera: the Omineca and Foreland belts (Fig. 1a). The profile is relatively crooked, with up to 30 km deviation from the best-fitting straight line, and there is considerable topographic relief, from 0.40 to 2.05 km above sea level. There were eight explosive shots recorded by an array of 270 portable seismographs. As such, this data set represents a typical continental crustal-scale wide-angle survey, although it is somewhat sparse in terms of shots and receivers by current standards. The traveltime picks consist of two refracted phases, P_g through the upper crust and P_n through the uppermost mantle, and two reflected phases, P_iP from an intracrustal boundary and P_mP from the crust–mantle (Moho) boundary (Figs 2a and 3a). There are 1165 refracted picks and 519 reflected picks (Table 1). P_iP is only observed from three shots. P_n is only observed from the two end shots, and for the western end shot P_n is only approximately 40 km in length, approximately 10 km of this as a later arrival behind P_g, making P_n nearly unreversed. For the eastern end shot, P_n is observed as a later arrival behind P_g for approximately 30 km.

The final preferred model for each data set in this paper was obtained using the Zelt & Smith (1992) algorithm. For the southeastern Canadian Cordillera data, the model was obtained in three layer-stripping steps as detailed by Zelt & White (1995). The starting model in each step was laterally homogeneous. The model parametrization is presented in Fig. 2(a) and the model is presented in a colour display in Fig. 4(a). The model consists of six layers, the first three representing the upper crust, the fourth the mid crust, the fifth the lower crust and the sixth the upper mantle (Fig. 2a). There are 50 and 34 independent velocity and boundary nodes, respectively, not counting those nodes at the edges of the model that are not constrained. The P_g phase constrains the three upper crustal layers. The two boundaries between the second, third and fourth layers at 2.2 and 11.9 km depth have no associated velocity discontinuity, and serve only to allow a variation in vertical velocity gradient; the boundary at 2.2 km depth also allows a lateral velocity variation at this depth (Fig. 2a). P_n is modelled using only headwaves, so there is no velocity constraint at depth within the uppermost mantle (Figs 3a and 4a). The final rms traveltime misfit and normalized χ^2 misfit are 67 ms and 1.86, respectively (Table 1). The final χ^2 value is greater than the ideal value of unity (Zelt 1999) because it would require adding many more model parameters, primarily in the upper crust, to fit the data, and in doing so it is not possible to achieve an acceptable resolution of, and constraint on, the model parameters. This is a result of a data set with fairly small picking uncertainties combined with relatively few shots and small-scale structure that it cannot resolve well (Zelt & White 1995).

3.2 Central India

The wide-angle data from central India between the towns of Hirapur and Mandla were acquired in 1983–84 by the Deep Seismic Sounding group of the National Geophysical Research Institute of India. The purpose of the survey was to determine the velocity structure across the Narmada-Son lineament and relate it to the

Downloaded from https://academic.oup.com/gji/article/153/3/609/671989 by U.S. Department of Justice user on 16 August 2022

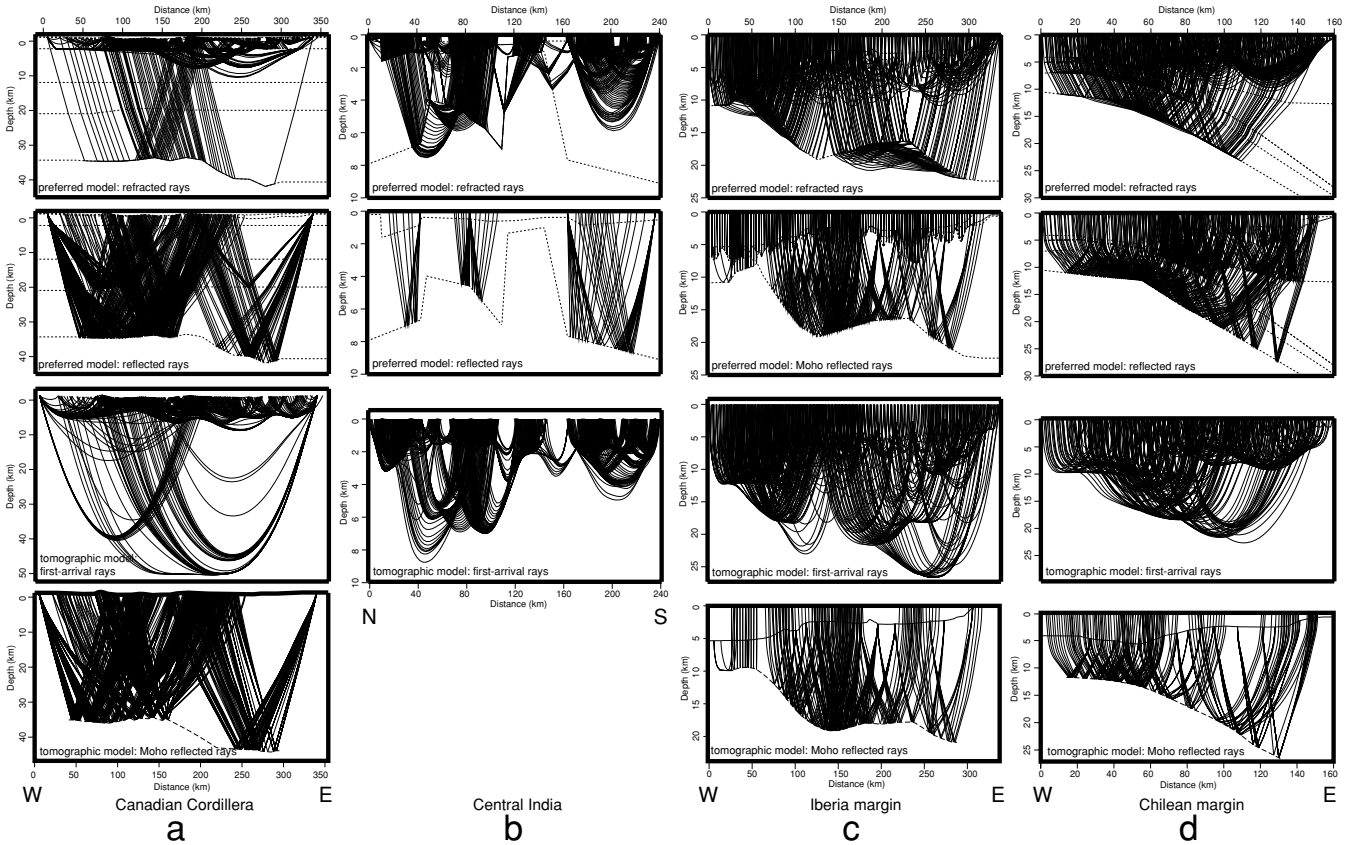

Figure 3. Raypaths through the preferred and tomographic models. (a) Southeastern Canadian Cordillera; (b) central India; (c) Iberia margin; (d) Chilean margin. The top two diagrams are for the refracted/headwave and reflected raypaths through the preferred model. The lower two diagrams are for the first-arrival and Moho reflected raypaths through the tomographic model; there are no Moho reflected raypaths for the Indian data set in (b). The dashed lines in the top two diagrams are layer boundaries. The solid and dashed lines in the bottom diagrams are the seafloor (c and d only) and Moho, respectively. The raypaths have been uniformly decimated for each data set for clarity.

tectonics of the area (Kaila *et al.* 1987, 1989; Sain *et al.* 2000). The NE–SW-trending Narmada-Son lineament is an ancient zone of weakness through which the Indian shield has undergone upwarp and subsidence several times in the geological record (West 1962; Ahmed 1964; Choubey 1971; Ghosh 1976). It divides the Indian landmass into two parts: the northern part covered by the Precambrian Vindhyan sediments and the southern part masked by the Cretaceous Deccan Traps (Fig. 1b). There are 16 shot points and 975 receivers at a nominal spacing of 200 m, from which 3912 first arrivals were picked from all shots and 85 wide-angle reflections were picked from four shots (Figs 2b and 3b; Table 1). From geological considerations and apparent velocities, the first arrivals were divided into three segments corresponding to three layers; the wide-angle reflections are from the basement, represented by the third layer. The first and second layers represent different geological units in the north and south sides of the model, as described below.

The data along the Hirapur-Mandla profile were inverted by Sain *et al.* (2000) using a whole-model approach and the algorithm of Zelt & Smith (1992). A 2-D starting model was used based on combining the results of a 1-D analysis of several shots. A three-layer model of upper crustal velocity and interface structure was obtained, specified by an irregular grid of 43 velocity nodes and 21 boundary nodes (Fig. 2b). The final rms traveltime misfit and normalized χ^2 misfit are 34 ms and 1.05, respectively (Table 1). The first and second layers, although continuous across the model, are interpreted as representing the Vindhyan sediments to the north and the Deccan Traps to the south (Fig. 5a; Sain *et al.* 2000).

3.3 Iberia margin

Both wide-angle and coincident MCS data from the Iberia margin were acquired along several profiles in 1997 by scientists from Rice University, The University of Texas at Austin, and GEOMAR, Germany (Sawyer *et al.* 1998; Zelt *et al.* 2003). The 335 km long dip profile crosses the Galicia Interior Basin, Galicia Bank, Galicia Bank Basin and the Peridotite Ridge (Fig. 1c). The portion of the profile across the Galicia Bank Basin includes the *S* reflector that forms the base of faulted and tilted basement blocks, and in some way appears to have played an important role in the evolution of the margin. The purpose of the survey was to image the margin structure from the coast to unambiguous oceanic crust to determine the mode of extension associated with the formation of the Iberia passive margin. The MCS data provide a detailed image of the margin sediments and basement, dominated by large tilted fault blocks (Unger 2001), but these data have penetration and multiple problems for deeper imaging. On the other hand, the wide-angle data provide good constraint on the subsedimentary velocity structure. Therefore, zero-offset reflection times from the sediments, basement and *S* reflector were inverted simultaneously with the deeper crustal and upper-mantle wide-angle phases to account for the

Downloaded from https://academic.oup.com/gji/article/153/3/609/671989 by U.S. Department of Justice user on 16 August 2022

Table 1. Data, model and inversion statistics and parameters.

	Southeastern British Columbia	Central India	Iberia Margin	Central Chilean Margin
Shots	8	16	335[1]	160[1]
Seceivers	270	975	26	20
Preferred model				
Refracted picks (average σ, ms)	1165 (64)	3912 (32)	2920 (149)	1344 (100)
Reflected picks (average σ, ms)	519 (95)	85 (40)	536 (164)	735 (115)
MCS picks (average σ, ms)	0	0	209 (50)	0
Layers	6	3	6	9
Velocity, boundary nodes	50, 34	43, 21	31[2], 19[3]	70, 43
$T_{\rm rms}$ (ms), χ^2 (final model)	67, 1.86	34, 1.05	116, 1.03	91, 0.88
First-arrival tomography				
First-arrival picks (average σ, ms)	1119 (63)	3912 (32)	2920 (149)	1070 (95)
$nx \times nz$ (finite-difference grid)	355 × 64	485 × 30	453 × 41	321, × 61
Node spacing (km)	1.0	0.5	0.75	0.5
Cell size, inverse grid (km)	2.0 × 1.0	1.0 × 0.5	1.5 × 0.75	1.0 × 0.5
Slowness cells	11 151	7018	9040	9600
Non-linear iterations	17	9	9	6
$T_{\rm rms}$ (ms), χ^2 (starting model)	327, 54.7	198, 35.7	403, 15.4	754, 64.7
$T_{\rm rms}$ (ms), χ^2 (final model)	67, 2.02	32, 1.00	104, 1.01	84, 0.95
Reflection tomography				
Reflection picks (average σ, ms)	425 (97)		550 (166)	153 (113)
Shots (land data) or	6		16 (OBS/H)	17
Receivers (marine data) used[4]			10 (MCS)[5]	
Node spacing (km)	1.0		0.75	0.5
Interface nodes	355		453	321
Non-linear iterations	6		3	5
$T_{\rm rms}$ (ms), χ^2 (starting model)	522, 51.2		540, 29.9	994, 80.6
$T_{\rm rms}$ (ms), χ^2 (final model)	84, 1.40		130, 1.00	111, 1.01

[1]Traveltime data were binned to provide an effective shot spacing of approximately 1 km; gaps in the original picks larger than 1 km were maintained; original airgun shot spacing is 100–150 m.
[2]There are 56 additional velocity nodes parametrizing the sediment layers, primarily constrained by the MCS data.
[3]There are 238 additional boundary nodes parametrizing the sediment layers, including the basement, primarily constrained by the MCS data.
[4]Not all shots for the land data or all receivers for the marine data yielded Moho reflection picks.
[5]10 picks from the MCS data of the *S* reflector were inverted along with the Moho reflection picks from the OBSs/OBHs.

complex shallow structure on the deeper raypaths (Zelt *et al.* 2003; Fig. 2c).

The wide-angle data have been picked from 26 ocean-bottom receivers (vertical component seismometers and hydrophones) that recorded airgun shots fired every 100–150 m. The wide-angle phases are unclassified first arrivals, corresponding to refractions within the sediments, crust and uppermost mantle, and reflections from the Moho (Figs 2c and 3c). There are 2920 and 536 refracted and reflected picks, respectively, after binning the picks using a 1 km spacing (Table 1). The zero-offset MCS picks from the base of the post-, syn- and pre-rift sediments and the *S* reflector (Figs 2c and 3c) were interpolated to a 3 km spacing to provide a total of 209 picks. The wide-angle and zero-offset picks were inverted simultaneously using the Zelt & Smith (1992) algorithm to obtain a six-layer velocity model, including the water layer, three sediment layers, and single crust and mantle layers (Zelt *et al.* 2003; Figs 2c and 6a). The water velocity and bathymetry were known *a priori*, and fixed. To match the MCS data, the sediment layers and basement were finely parametrized, including several pinchouts and steep boundaries (Fig. 2c), with lateral velocity and boundary node spacings of approximately 20 and 2.5 km, respectively, yielding a sediment model specified by 56 and 238 independent velocity and boundary nodes. By comparison, the subbasement model is specified by only 31 and 19 velocity and boundary nodes. In the starting model, the sediment layers and basement were designed to match the MCS traveltimes using a constant velocity in each layer based on averaging the results from the velocity analysis of several CMP gathers; the subbasement crustal and mantle layers were laterally homogeneous (Zelt *et al.* 2003). The first arrivals, indicated as P_s, P_g and P_n in Fig. 2(c), were treated as one phase by the inversion scheme, matching each pick with the earliest predicted time from any of the model layers. Both headwaves and refractions were traced through the upper mantle (Fig. 3c). The final rms traveltime misfit and normalized χ^2 misfit are 116 ms and 1.03, respectively (Table 1); the relatively large pick uncertainties are due to much of the data having a low signal-to-noise ratio.

3.4 Chilean margin

The wide-angle data from the Chilean margin were collected in 1995 by GEOMAR (Flueh *et al.* 1998) in a region where the aseismic Juan Fernández Ridge on the Nazca Plate is subducting beneath South America (von Huene *et al.* 1997, Fig. 1d). In addition to two 2-D dip profiles, 3-D data were also acquired (Zelt *et al.* 1999). The purpose of the survey was to image the large-scale margin structure and establish the relationship between seamount subduction, plate deformation and seismicity patterns. A magnetic anomaly at the

Downloaded from https://academic.oup.com/gji/article/153/3/609/671989 by U.S. Department of Justice user on 16 August 2022

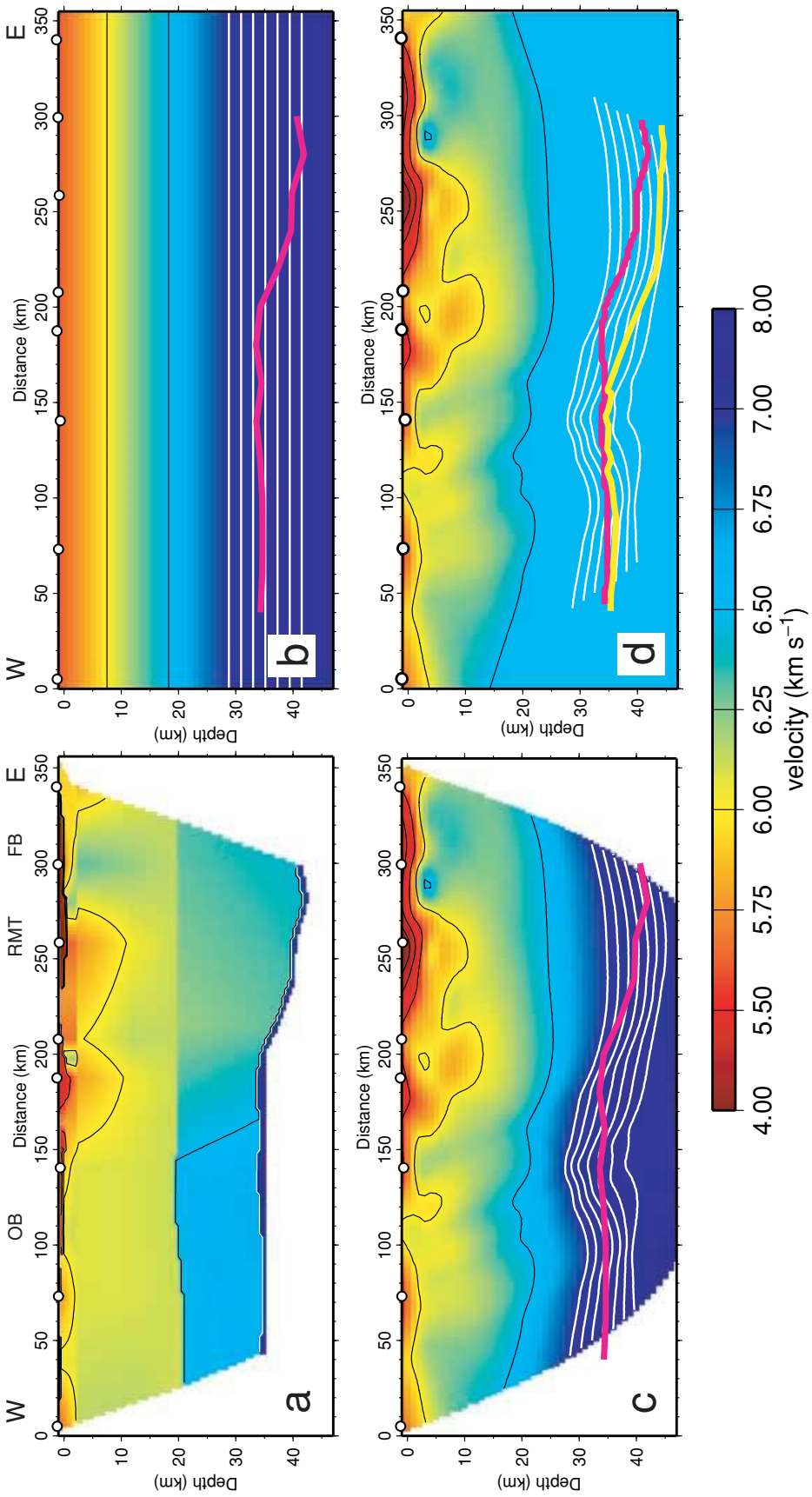

Figure 4. Models for the southeastern Canadian Cordillera data. (a) Preferred model; (b) starting model for first-arrival tomography; (c) final tomographic velocity model; (d) velocity model for reflection tomography with the reflection tomography Moho indicated by a yellow line. Only those portions of the preferred and final tomographic velocity and Moho models sampled by raypaths are shown. Pink line in (b)–(d) is the preferred Moho. Black contours between 4.5 and 6.5 km s^{-1} have an interval of 0.5 km s^{-1}; white contours correspond to 7.0–7.6 km s^{-1} in 0.1 km s^{-1} intervals; white contours in (d) are from the tomographic velocity model. Shot point locations indicated by circles; only those shots points with Moho reflections shown in (d). The Omineca Belt (OB), Rocky Mountain Trench (RMT) and Foreland Belt (FB) are labelled above the preferred model. Note the non-linear scale bar for velocity.

Downloaded from https://academic.oup.com/gji/article/153/3/609/671989 by U.S. Department of Justice user on 16 August 2022

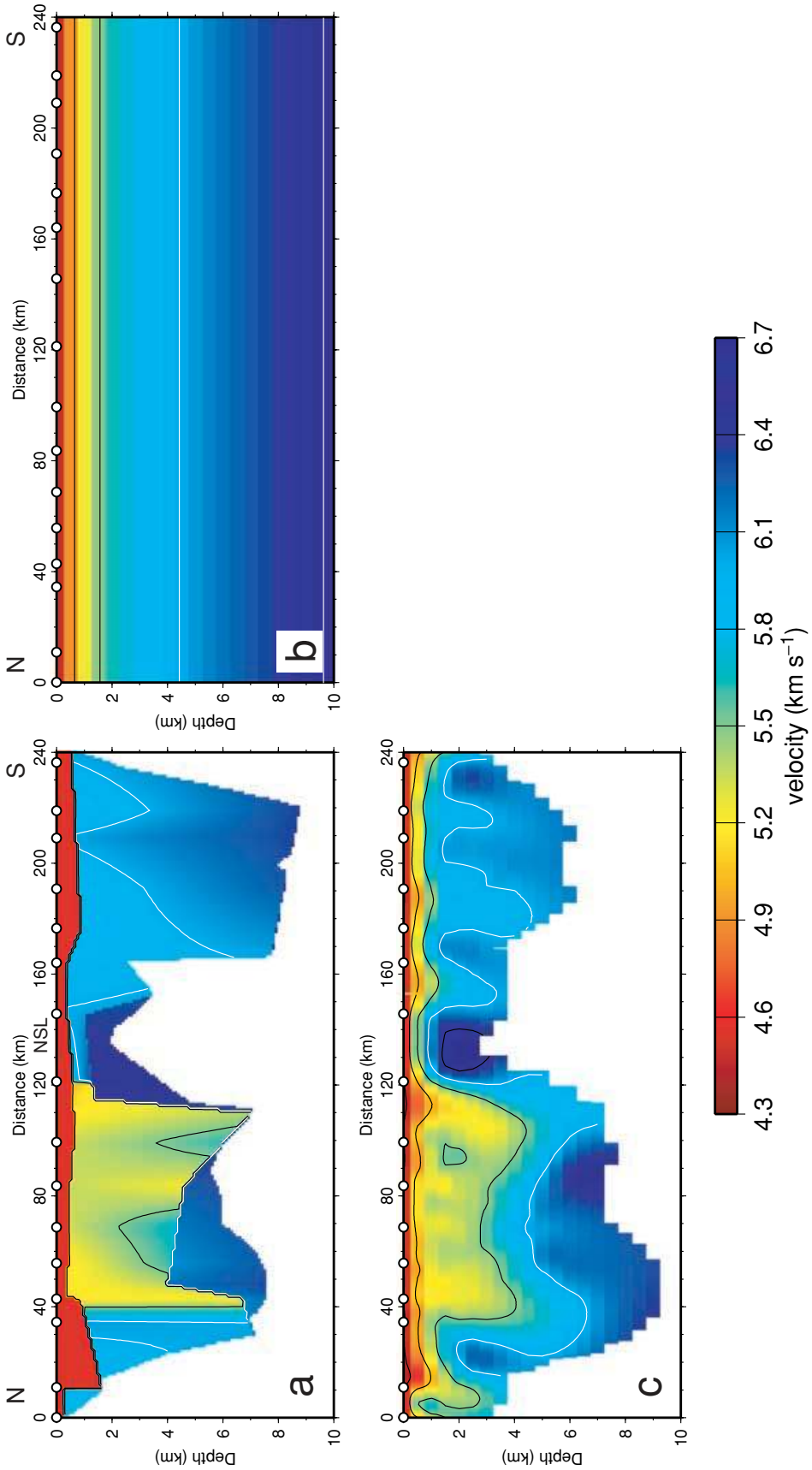

Figure 5. Models for the central India data. (a) Preferred model; (b) starting model for first-arrival tomography; (c) final tomographic velocity model. Black contours between 4.5 and 5.5 km s^{-1} have an interval of 0.5 km s^{-1}; white contours correspond to 6.0 and 6.5 km s^{-1}. Only those portions of the preferred and final tomographic velocity models sampled by raypaths are shown. Shot point locations indicated by circles. The Narmada-Son Lineament (NSL) is labelled above the preferred model.

Downloaded from https://academic.oup.com/gji/article/153/3/609/671989 by U.S. Department of Justice user on 16 August 2022

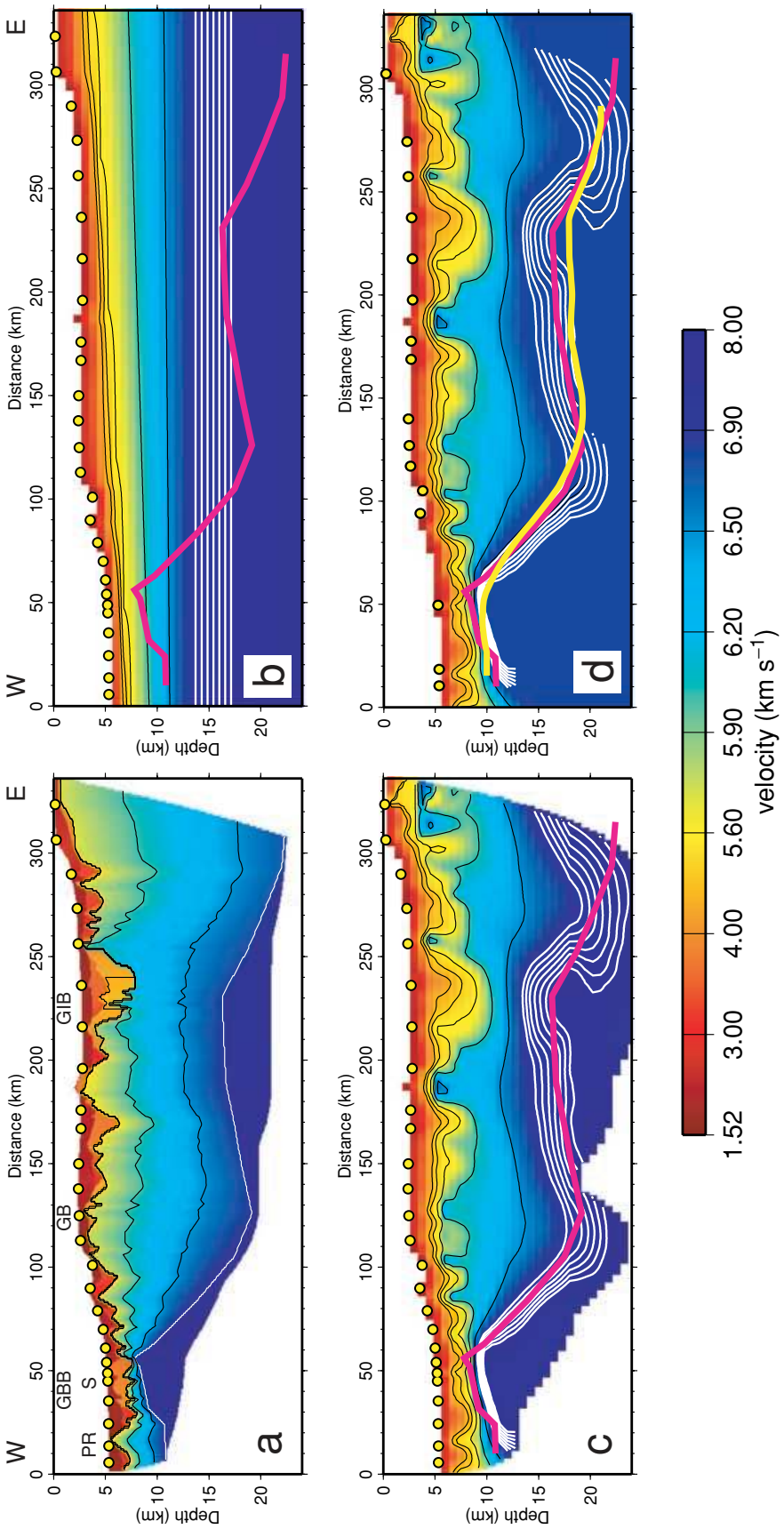

Figure 6. Models for the Iberia margin data. (a) Preferred model; (b) starting model for first-arrival tomography; (c) final tomographic velocity model; (d) velocity model for reflection tomography with the reflection tomography Moho indicated by a yellow line. Only those portions of the preferred and final tomographic velocity and Moho models sampled by raypaths are shown. Pink line in (b)–(d) is the preferred Moho. Black contours between 4.5 and 6.5 km s^{-1} have an interval of 0.5 km s^{-1}; white contours correspond to 7.0–7.6 km s^{-1} in 0.1 km s^{-1} intervals; white contours in (d) are from the tomographic velocity model. Ocean-bottom receiver locations indicated by circles; only those ocean-bottom receivers with Moho reflections shown in (d). The Peridotite Ridge (PR), *S* reflector (S), Galicia Bank Basin (GBB), Galicia Bank (GB) and Galicia Interior Basin (GIB) are labelled above the preferred model. Note the non-linear scale bar for velocity.

Downloaded from https://academic.oup.com/gji/article/153/3/609/671989 by U.S. Department of Justice user on 16 August 2022

northern edge of the survey area has been interpreted as indicating the subducted Papudo seamount (von Huene *et al.* 1997, Fig. 1d).

The northern 160 km long dip profile at ∼33°S was shot obliquely over the Juan Fernández Ridge using an airgun shot spacing of 100–150 m and 20 ocean-bottom receivers. This profile extends from normal oceanic crust across the Chile Trench to the Valparaiso forearc basin on the trench slope (Fig. 1d). A large number of refracted and reflected arrival types were picked and classified according to layer for the development of the preferred model (Fig. 2d) using the Zelt & Smith (1992) algorithm and a bootstrap approach in which the model was progressively built up, adding picks for which the identification was increasingly less certain at each stage (Naumenko 2001). The refracted arrivals turn within layers representing the slope and oceanic sediments, oceanic layers 2 and 3, the accretionary wedge, the continental upper crust and the oceanic uppermost mantle. The reflected arrivals come from the top of the accretionary wedge, subducted sediments, oceanic layer 2, a sediment layer within the Valparaiso basin, basement, continental lower crust and the uppermost mantle (Figs 2d and 3d). A starting model was developed using the known bathymetry, the sediment thickness from coincident reflection lines (von Huene *et al.* 1997), the nearest 2-D *P*-wave velocity model along the margin at ∼24°S (Comte *et al.* 1994) and the dip of the subducting plate to 60 km depth (15°) based on regional seismicity (Tichelaar & Ruff 1991). The preferred model has nine layers and 70 and 43 velocity and boundary nodes, respectively (Fig. 2d). The picks were binned at a 1 km spacing from the original airgun shot interval, to yield a total of 1344 refracted picks and 735 reflected picks (Table 1). The final rms traveltime misfit and normalized χ^2 misfit are 91 ms and 0.88, respectively (Table 1); the slight overfit was unintentional, and is a result of being able to fit the data well using a model that includes all the structure required by the prior information, without much additional shorter-wavelength structure (Fig. 7a). The approach for developing the starting model and the simultaneous refraction and reflection inversion were designed to exploit and honour the available prior information and use as much of the wide-angle data as possible.

4 MODEL ASSESSMENT: REFRACTION TOMOGRAPHY

The algorithm of Zelt & Barton (1998) is used for refraction tomography in which the model is parametrized using a uniform grid of velocity nodes for the forward calculation, and a rectangular grid of constant-slowness cells for the inverse step. The first-arrival times are calculated using a finite-difference solution to the eikonal equation based on the method of Vidale (1988), and modified to accurately handle large velocity contrasts using the approach of Hole & Zelt (1995). A best-fitting laterally homogeneous (1-D) starting model is typically used and model updates are determined over several iterations, in which new raypaths are calculated at each iteration, until the observed traveltimes are ideally fitted with a normalized misfit (χ^2) of unity (Zelt & Barton 1998).

The goal of refraction tomography as we have applied it is to derive the simplest, i.e. most featureless, model that appropriately fits the first-arrival times. As is common in traveltime tomography, we have chosen to equate simplest with smoothest (e.g. Lees & Crosson 1989; Scales *et al.* 1990). Roughness, the inverse of smoothness, is measured using the second spatial derivative of the discretized slowness values (Zelt & Barton 1998). The subjective free parameters in the Zelt & Barton (1998) approach are: (1) the starting model, (2) the forward and inverse model grid spacing, (3) the initial trade-off parameter in the objective function that weighs the relative importance of overall data misfit and model roughness, (4) the weighting factor that determines the importance of minimizing vertical versus horizontal model roughness and (5) the number of iterations of the conjugate gradient, sparse linear system solver (Nolet 1987) applied at each non-linear iteration of the inversion.

A 1-D starting model can be determined by either laterally averaging the preferred model, if one already exists, or by laterally averaging the final model obtained from a tomographic inversion in which an initial 1-D starting model is used based on an inspection of the time-offset pattern of the observed data as a whole, or for selected shots or receivers. In either case, the 1-D model is smoothed vertically to remove any 'layering' (velocity discontinuities), which may bias the results, to the extent possible so that the observed data are fitted as well as possible by a 1-D model. For the four data sets under consideration here, both approaches were used to yield what we consider to be approximately the most featureless 1-D starting models that are capable of providing geologically reasonable results (Fig. 8). For the Canadian Cordillera data, a linear-gradient starting model, with 10 km of zero-gradient padding at the bottom (Fig. 8a) to prevent rays from reaching the bottom of the model, yielded satisfactory results. The starting model for the Indian data is very smooth, with the largest change in gradient occurring near 2 km depth (Fig. 8b). For the Iberia and Chilean data, pseudo-1-D starting models were used because of the large variation in water depth (over 5 km) along each profile (Figs 6 and 7). In each case, the shallow subseafloor velocity structure was made to conform to the known bathymetry with a transition to horizontal lateral homogeneity reached at 12 and 10 km depth, respectively (Figs 6b and 7b). Reduced vertical velocity gradients near the bottom of both models were again used for padding.

The node spacing used by the finite-difference method for the forward calculation of traveltimes must be equal in the horizontal and vertical directions (Vidale 1988). The spacing is chosen for each data set so that sufficiently accurate traveltimes are calculated relative to the picking uncertainties. Experience working with many data sets suggests that a suitable number of nodes horizontally is approximately 300, and this can be checked by running a test using a smaller node spacing to ensure that the predicted times do not change significantly relative to the picking uncertainties. For the data sets in this paper, node spacings of 0.5–1.0 km are used, resulting in between 321 and 485 nodes across the length of the models (Table 1). The model parametrization for the inverse step is cell-based in which the cell dimensions must be multiples of the forward grid node spacing, but the cells can be rectangular with unequal horizontal and vertical dimensions (Zelt & Barton 1998). A suitable cell size is one that allows the data to be fitted appropriately, with a normalized misfit of 1.0 (Zelt 1999). For all four data sets, the cell sizes are twice the horizontal forward node spacing, and equal to the vertical forward node spacing, resulting in cell sizes of 1.0 × 0.5 to 2.0 × 1.0 km for the inverse grids (Table 1). Using smaller cell sizes than that required to fit the data is not a problem, except for the added CPU time, since the smoothing regularization keeps the results stable. One exception to the rule of fitting the data with a normalized misfit of 1.0 was the Canadian data set, in which a cell size was chosen that allowed the same rms traveltime misfit as the preferred model (Table 1) so that an appropriate comparison between the tomographic and preferred models could be made.

The initial trade-off parameter in the objective function is determined by trial and error for each data set so that the rms traveltime misfit decreases by 10–30 per cent after the first non-linear iteration. This reduces the chances that the inversion will take too large a step

Downloaded from https://academic.oup.com/gji/article/153/3/609/671989 by U.S. Department of Justice user on 16 August 2022

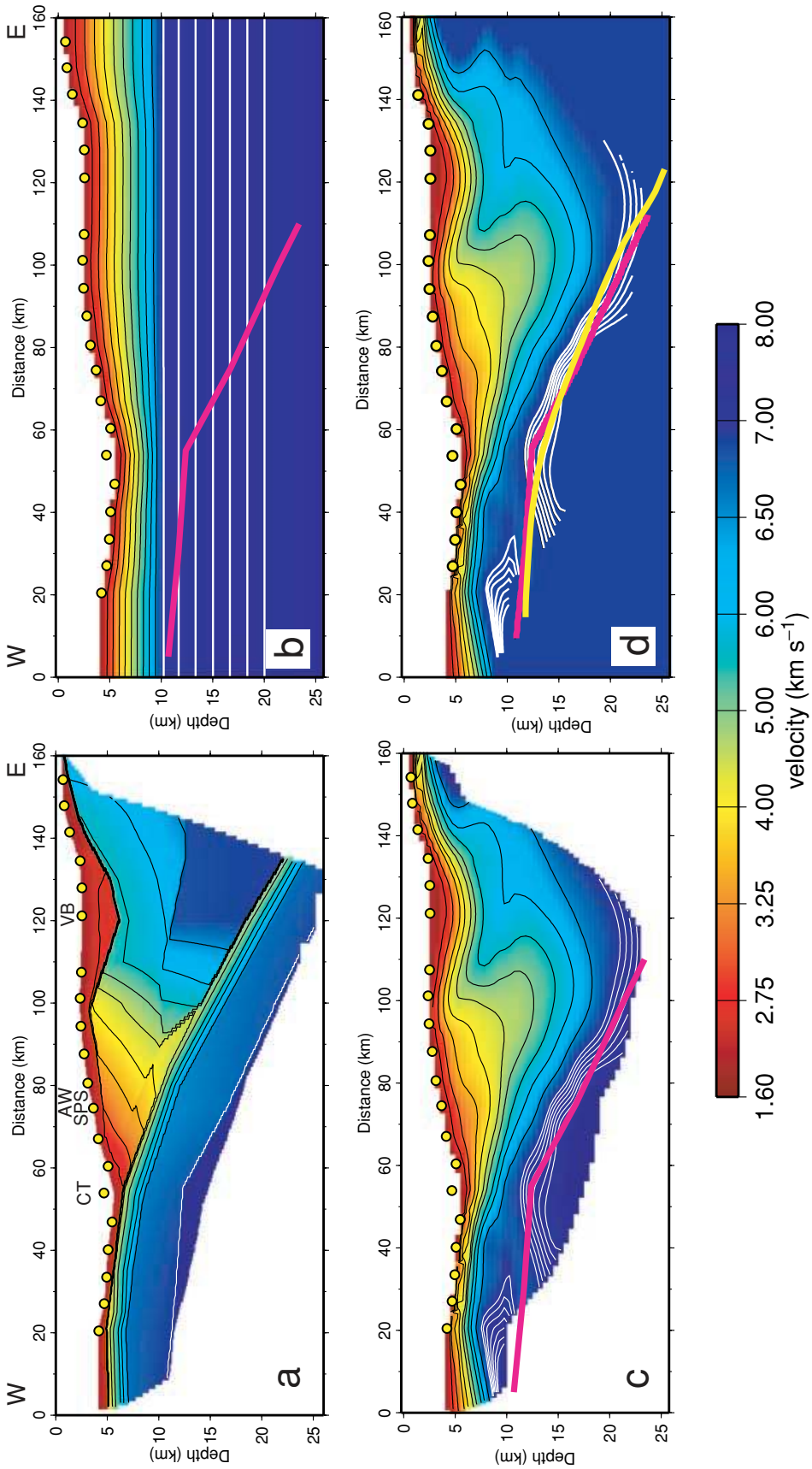

Figure 7. Models for the Chilean margin data. (a) Preferred model; (b) starting model for first-arrival tomography; (c) final tomographic velocity model; (d) velocity model for reflection tomography with the reflection tomography Moho indicated by a yellow line. Only those portions of the preferred and final tomographic velocity and Moho models sampled by raypaths are shown. Pink line in (b)–(d) is the preferred Moho. Black contours between 2.5 and 6.5 km s^{-1}; white contours correspond to 7.0–7.6 km s^{-1} in 0.1 km s^{-1} intervals; white contours in (d) are from the tomographic velocity model. Ocean-bottom receiver locations indicated by circles; only those ocean-bottom receivers with Moho reflections shown in (d). The Chile Trench (CT), Subducted Papudo Seamount (SPS), Accretionary Wedge (AW) and Valparaiso Basin (VB) are labelled above the preferred model. Note the non-linear scale bar for velocity.

Downloaded from https://academic.oup.com/gji/article/153/3/609/671989 by U.S. Department of Justice user on 16 August 2022

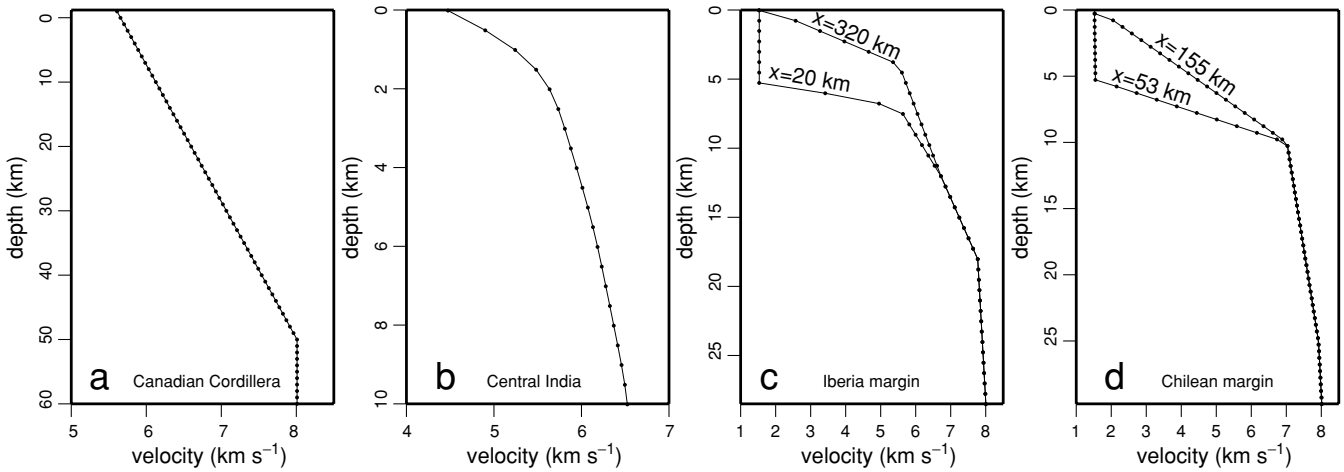

Figure 8. 1-D or pseudo-1-D starting models for the first-arrival tomographic inversion. (a) Southeastern Canadian Cordillera; (b) central India; (c) Iberia margin; (d) Chilean margin. Dots indicate node spacing for forward calculation of traveltimes using an eikonal solver; vertical cell size for the inverse step is the same as the node spacing in each case. For (c) and (d) the upper portion of the starting models are adapted to the bathymetric variations (Figs 6b and 7b), and velocity–depth profiles at two x positions are indicated as labelled.

in model space, thereby violating the assumptions of the linearization, and possibly getting trapped in a local minima. The vertical smoothing weighting parameter is chosen rather subjectively, but experience with many crustal wide-angle data sets have shown that values between 0.1 and 0.3 typically give the most geologically reasonable results. The values used in this paper are 0.2, 0.125, 0.25, 0.15 for the data from the Canadian, Indian, Iberia and Chilean data, respectively. The number of iterations of the linear system solver at each non-linear iteration of the inversions was 100 for all data sets, yielding a good compromise between sufficiently accurate and smooth model updates and minimal CPU time. As pointed out by several authors, it is only necessary to approximately solve the linear system at each non-linear iteration, since the linearization is itself an approximation (e.g. McCaughey & Singh 1997). Perhaps most important is that extensive tests with the data in this paper and other data, have shown that the final results are relatively insensitive to moderate changes in all five free parameters, including roughly a factor of 2 variation in the values of the initial trade-off parameter in the objective function, the weighting factor that controls the vertical versus horizontal roughness and the number of iterations of the sparse linear system solver.

The total number of cells comprising the inverse model parametrizations are between approximately 7000 and 11 000 (Table 1), in each case being greater than the number of picks inverted. The ratio of cells to picks varies between 1.8 for the Indian data to 10.0 for the Canadian data. It is the smoothing regularization that provides the additional constraint on the model parameters to keep the inversions stable and the final models smooth. For the Canadian and Chilean data sets, the number of first-arrival picks used in the tomographic inversion is less than the refracted picks used to derive the preferred model (Table 1). This is because 4 per cent of the Canadian refracted picks and 20 per cent of the Chilean refracted picks are not first arrivals. The number of non-linear iterations of the tomographic inversion required to achieve the final models varies between 6 and 17, dropping the rms traveltime misfits from the starting models to the final models by factors of between 3.9 and 9.0 (Table 1). The final normalized misfit (χ^2) is approximately unity for each data set, except for the Canadian data as described earlier.

5 MODEL ASSESSMENT: REFLECTION TOMOGRAPHY

The algorithm of Zelt *et al.* (1999) is used for reflection tomography, except that only one reflected phase (P_mP) and one interface (the Moho) is involved and the velocity model is fixed. For the forward and inverse steps, the Moho is parametrized using a uniform node spacing equal to the forward velocity grid node spacing (Table 1). The reflection times are calculated using a finite-difference solution to the eikonal equation based on the method of Hole & Zelt (1995). A flat starting model is used and, as with the refraction tomography, model updates are determined over several iterations, in which new raypaths are calculated at each iteration, until the observed P_mP traveltimes are predicted by the model with a normalized misfit (χ^2) of unity. Again, one exception to this is the Canadian data, in which an rms P_mP misfit similar to that provided by the preferred model was sought (Table 1).

The inversion of the first arrivals and P_mP was decoupled using the former to solve for the velocity model, and the latter to solve only for the Moho geometry keeping the velocity field fixed; note that the velocity models have their own expression of the Moho, albeit as a smooth transition zone (Figs 4c, 6c and 7c). The first arrival and P_mP inversions were decoupled for several reasons: (1) because the confidence with which we can identify and picked reflected phases is usually much less than for first arrivals, and we want to avoid corrupting the tomographic velocity model with P_mP data, (2) to independently assess the type of Moho structure required by the refraction and reflection arrivals, and produce two tomographic Mohos to compare with the Moho in the preferred model, (3) this is a more objective approach that does not assume that P_n refracts directly beneath the interface from which P_mP reflects; for example, the Moho could be a transition zone in which the P_mP picks correspond to the top of the zone and P_n refracts from the bottom and (4) this is the opposite approach used to obtain the preferred models, and for the purpose of model assessment it is generally most instructive to use opposite, end-member approaches as advocated by Zelt (1999).

As with refraction tomography, the goal of reflection tomography is to derive the most featureless model (Moho) that fits the arrival times (P_mP). We tried solving for both the smoothest and flattest

Downloaded from https://academic.oup.com/gji/article/153/3/609/671989 by U.S. Department of Justice user on 16 August 2022

Moho and found they were similar, but we prefer the flattest models because they have less structure at the ends of the models and in regions in between where there is no ray coverage; a flattest inversion involves minimizing the first spatial derivative of the Moho. The subjective free parameters in reflection tomography are: (1) the starting model, (2) the forward/inverse node spacing, (3) the initial trade-off parameter in the objective function that weighs the relative importance of overall data misfit and model structure and (4) the number of iterations of the conjugate gradient routine applied at each non-linear iteration of the inversion.

A suitable horizontal starting model for the Moho can readily be determined by trial and error as that which gives the best overall fit to the observed P_mP data. For the data sets under consideration here, the starting models have depths of 36 km for the Canadian data, and 15 km for both the Iberia and Chilean data; the Indian data do not sample deep enough to reach the Moho. As mentioned above, the node spacing used by the algorithm for the forward and inverse model parametrizations equals the forward velocity grid node spacing, between 0.5 and 1.0 km for the data sets under consideration (Table 1). The regularization keeps the inversion stable even for data sets with relatively few reflection picks or gaps in coverage. The selection of the initial trade-off parameter in the objective function and the number of iterations of the linear system solver at each non-linear iteration are treated in the same way as for the refraction tomography.

To perform reflection tomography it is first necessary to edit the velocity model obtained from refraction tomography to remove the upper-mantle 'layer'. This is necessary because *a priori* we do not know to what depth the reflection Moho will sink during the inversion and we do not want the velocity nodes above the Moho interface to correspond to upper-mantle values. To remove the upper mantle from the tomographic velocity model, we simply reset the value of any velocity node in the model that has a value greater than the average velocity at the base of the crust in the preferred model. This value is 6.5, 6.8 and 6.9 km s^{-1} for the Canadian, Iberia and Chilean models. If there is a concern about the bias introduced by using the preferred model as a guide, a range of values for the average lower crustal velocity could be tested and the resultant range of Mohos could be used for model assessment.

The total number of nodes comprising the parametrization of the Moho varies between 321 and 485, with the ratio of nodes to P_mP picks varying between 0.8 and 2.1 (Table 1). The number of shots (Canadian data) or OBSs (Iberia and Chilean data) for which it was possible to make P_mP picks is less than the total number of shots or OBSs comprising each data set, being 6, 16 and 17 for the three data sets, respectively. The number of non-linear iterations of the tomographic inversion required to reach the final models varies between 3 and 6, dropping the rms traveltime misfits from the starting models to the final models by factors of between 4.2 and 9.0 (Table 1). The final normalized misfit (χ^2) is approximately unity for the Iberia and Chilean data, but 1.4 for the Canadian data for the reasons described earlier.

6 RESULTS

The preferred and tomographic models for each data set are presented in Figs 4–7. Fig. 9 provides a more quantitative comparison of the velocity models along four horizontal and four vertical velocity profiles through each model. As expected, the tomographic models are smoother than the preferred models, although the tomographic velocities generally correspond well to a long-wavelength average of the preferred model. The vertical profiles in Fig. 9 show how the sharp layering in the preferred models is smoothed out in the tomographic models, in particular, there is no sharp expression of the basement or Moho in the tomographic models. Thus, for vertical variations, it is more meaningful to examine the isovelocity contours of the models in Figs 4(c)–7(c). By comparing each preferred and tomographic model, it is clear that the tomographic velocity models are best for checking the long-wavelength structure and relative velocity variations in the preferred models, as opposed to the velocity at a specific point.

The white isovelocity contours in the tomographic models in Figs 4, 6 and 7 correspond to the range of values that lie between the velocities at the base of the crust and the top of the upper mantle in the preferred models, 7.0–7.6 km s^{-1}. This allows for the appropriate comparison between the preferred Moho, modelled as a sharp velocity discontinuity, and the tomographic Moho from the first-arrival inversion, modelled within a smooth velocity field. The third model of the Moho is that obtained from the reflection tomography, and this boundary can be compared directly with the preferred Moho and the 7.0–7.6 isovelocity contours from the tomographic velocity model (Figs 4d, 6d and 7d).

The perturbations of the final tomographic velocity models with respect to the starting models are shown in Fig. 10. The perturbation plots reveal some structure that is not apparent in Figs 4(c)–7(c). The length-scales of the perturbations are a function of the resolution provided by the data, and the real subsurface structure. The perturbations of the Canadian and Iberia models have the longest and shortest average wavelengths, respectively, probably as a result of the relatively sparse and dense data, respectively. The Chilean perturbations are surprisingly large given the data density, but note that the Chilean model is approximately half the length of the Iberia model. For three data sets the perturbations reach a little more than 1 km s^{-1} in magnitude, but for the Chilean data they are as much as 2.4 km s^{-1}. These are large perturbations in both an absolute and relative sense, but there is no evidence that the refraction tomography has suffered from non-linear effects, such as sensitivity to the free parameters of the inversion, as one might expect for such large perturbations from the starting models.

6.1 Southeastern British Columbia

The most prominent features of the preferred model from the Canadian Cordillera are: (1) relatively low and high velocities in the upper crust between 150–260 and 270–320 km, respectively, (2) overall low velocities in the lower crust (6.2–6.7 km s^{-1}), with a decrease in lower crustal velocity by 0.3–0.4 km s^{-1} on the right half of the model beneath the Foreland belt compared with the left half beneath the Omineca belt and (3) approximately 7 km of crustal thickening over 80 km distance centred beneath the Rocky Mountain Trench in the Foreland Belt (Fig. 4a).

The tomographic velocity and Moho models contain similar versions of these features. In the upper crust, both velocity models include two lobes of relatively low velocity extending to approximately 10 km depth between 150–270 km, along with the high-velocity zone separating them reaching up to approximately 5 km depth at 210–220 km. Both models include a high-velocity portion of the upper crust to approximately 5 km depth between 275–300 km. The lateral velocity variation in the lower crust is also present in both models, but not in the same way. In the preferred model it appears as a rather sharp transition between approximately

Downloaded from https://academic.oup.com/gji/article/153/3/609/671989 by U.S. Department of Justice user on 16 August 2022

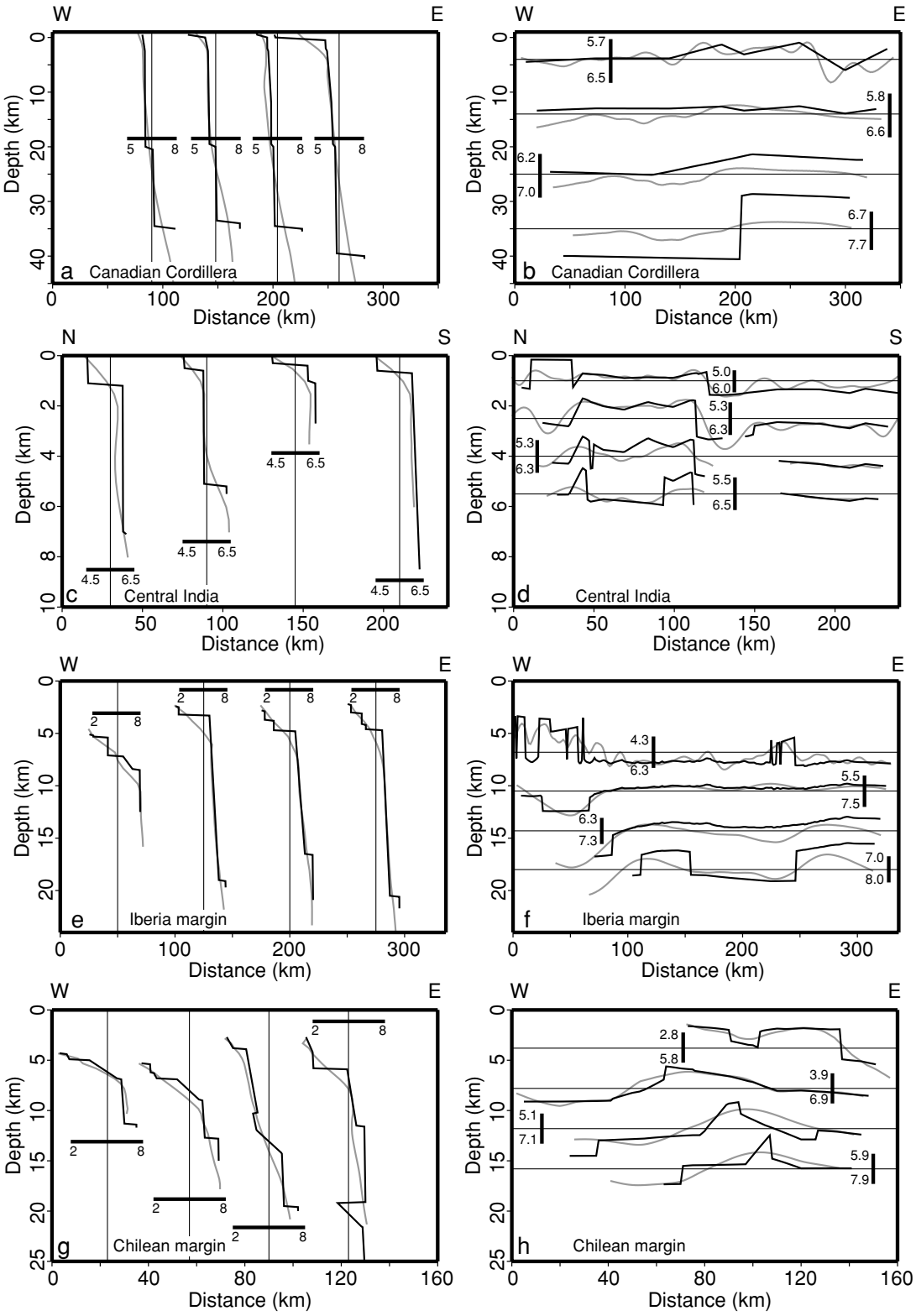

Figure 9. Comparison of the preferred and tomographic velocity models along four vertical slices and four horizontal slices. (a), (b) Southeastern Canadian Cordillera; (c), (d) central India; (e), (f) Iberia margin; (g), (h) Chilean margin. Vertical profiles are shown in the left column of figures; horizontal profiles in the right column. Thick black lines correspond to the preferred models; grey lines correspond to the tomographic models. Precise *x* and *z* position of each slice indicated by thin black line. The velocity scale for each slice indicated by the scale bar plotted perpendicularly along the slice and labelled with the velocity (km s^{-1}) corresponding to the ends of the scale bar; note that some velocity profiles vary beyond the limits of the corresponding scale bar. Each profile is limited to regions of the preferred and tomographic velocity models that are sampled by raypaths.

Downloaded from https://academic.oup.com/gji/article/153/3/609/671989 by U.S. Department of Justice user on 16 August 2022

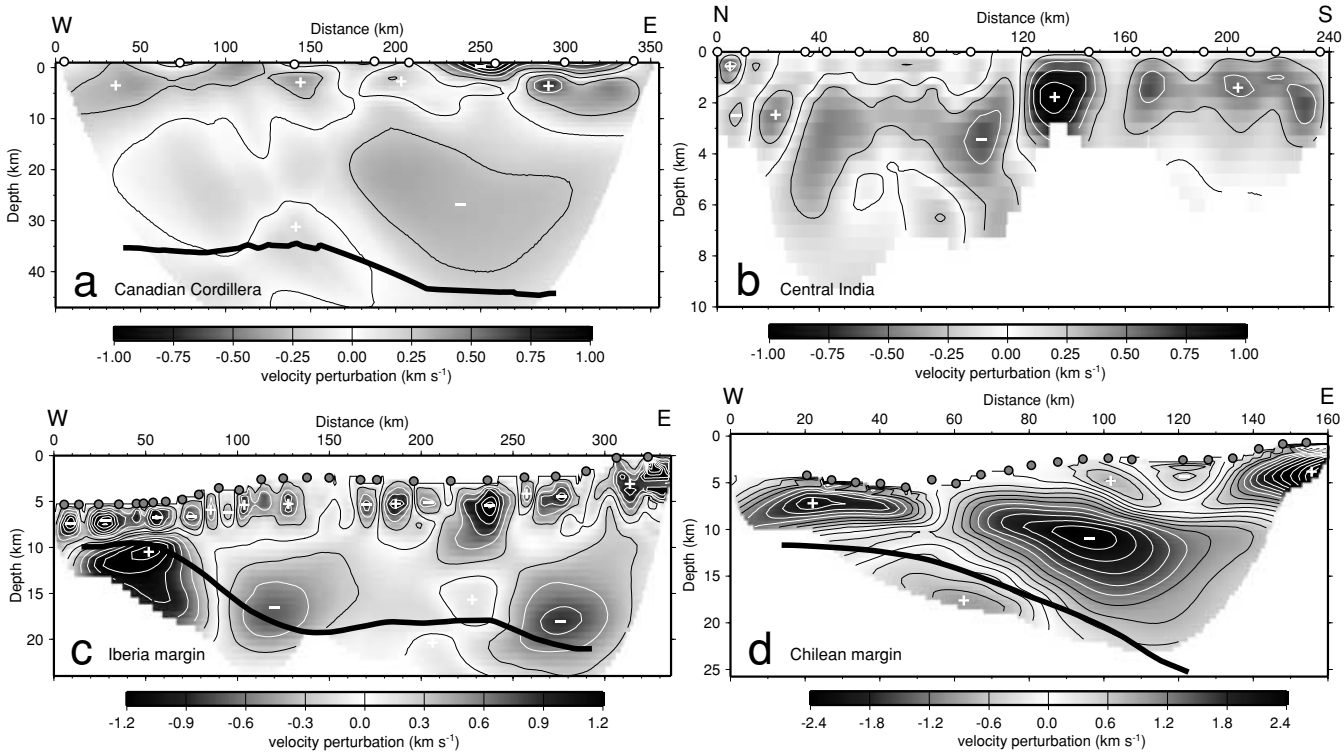

Figure 10. Perturbation of final tomographic velocity models with respect to the corresponding starting model. (a) Southeastern Canadian Cordillera; (b) central India; (c) Iberia margin; (d) Chilean margin. Thick black lines in (a), (c) and (d) is the Moho boundary from reflection tomography. Contour interval is 0.25 km s^{-1}; contours for perturbations greater in magnitude than 0.25 km s^{-1} are white, except in (d) where contours for perturbations greater in magnitude than 1.0 km s^{-1} are white. The sign of positive and negative anomalies are indicated by plus and minus signs. Shot point locations indicated by open circles; ocean-bottom receiver locations indicated by grey circles. Only those portions of the tomographic velocity and Moho models sampled by raypaths are shown. Different scale bars suited to each model have been used. This figure is in colour in the online version of the journal on *Blackwell Synergy.*

150–200 km, but in the tomographic model it appears more as a result of the isovelocity contours in the lower crust conforming to the thickened crust beneath the Foreland belt. The more subdued lateral velocity variation in the tomographic model is apparent in the horizontal slice at 25 km depth (Fig. 9b) and the perturbation plot in Fig. 10(a) clearly shows the lower crustal lateral velocity variation between 15 and 35 km depth. The thickened crust beneath the Foreland belt is clear in all three Moho models, although in both tomographic models it is shifted to the west by approximately 50 km. The extent of the thickening is slightly more in the reflection tomography Moho compared with the preferred Moho, but it is less in the tomographic velocity model. These differences can be explained by the more subdued lower crustal lateral velocity variation in the tomographic model and the resultant velocity–depth trade-off for the Moho. Finally, between 280–300 and 2.5–5 km depth, the tomographic model has a larger-amplitude, high-velocity anomaly than the preferred model. Since the P_g data are underfitted at the eastern end of the preferred model, the weaker anomaly in the preferred model suggests a stronger anomaly, as required to better fit the data, was considered geologically unreasonable.

6.2 Central India

The prominent features of the preferred model from central India are: (1) a thickening of Vindhyan sediments between 10–40 km up to 1.5 km deep, (2) the Vindhyan basin appears as a relatively low-velocity graben structure extending to 4–7 km depth between 40–120 km bounded by relatively steep faults and (3) a prominent high-velocity (∼6.5 km s^{-1}) basement horst beneath the Narmada-Son lineament and between the Vindhyan basin to the north and the Deccan Traps to the south at approximately 1.5 km depth between 110 and 150 km (Fig. 5a). The faults bounding the Vindhyan basin are modelled using a lateral velocity variation in layer 2 to the north, and a relatively steep layer boundary with a dip of ∼50° to the south against the horst (Fig. 2b).

Again, the tomographic velocity model contains similar versions of these features. The thickened Vindhyan sediments between 10–40 km are not as prominent in the tomographic model, but their northern edge at approximately 10 km is well defined. The Vindhyan basin is well expressed in the tomographic model, including similar steep sides, although it does not appear to extend quite as deep. Even the upwarped shape of the basement beneath the basin in the preferred model is apparent in the tomographic model, albeit more smoothly; the perturbation plot in Fig. 10(b) shows the upwarp clearly. The high-velocity horst is centred at nearly the same position, approximately 135 km, and is very close in velocity to that in the preferred model, ∼6.5 km s^{-1}, but it is approximately 10 km narrower in lateral extent in the tomographic model. The horst may appear to be narrower in the tomographic model because its edges are smoother compared with the sharp velocity discontinuities in the preferred model made possible by the layer boundary; this is best observed in the horizontal slices through the models at 2.5 km depth (Fig. 9d).

Downloaded from https://academic.oup.com/gji/article/153/3/609/671989 by U.S. Department of Justice user on 16 August 2022

6.3 Iberia margin

The most prominent features of the preferred model from the Iberia margin are: (1) the Peridotite Ridge exposed at or near the seafloor at 15 km model distance, (2) thinned crust between 30–55 km where the S reflector appears to be the Moho just 3–5 km beneath the seafloor and its seaward dip suggests it is a detachment fault (Unger 2001; Zelt *et al.* 2003), (3) a local maximum of approximately 19 km in Moho depth at 125 km and (4) a local minimum of approximately 16 km in Moho depth at 230 km, with a sediment thickness of up to 5 km above this between 215 and 255 km (Fig. 6a). Landward of the *S* reflector, the correlation between crustal thickness, water depth and sediment thickness is typical for a rifted margin (Fig. 6a). Crustal thickness variations suggest the margin was extended in two phases, spatially separated by approximately 100 km (Zelt *et al.* 2003).

The Peridotite Ridge is weakly expressed in the tomographic velocity model at the correct position; this is best observed in the horizontal slice through the models at 7 km depth (Fig. 9f). The seaward-dipping thinned crust between 30 and 55 km is well matched by the tomographic velocity model, slightly less so by the tomographic Moho, but both tomographic models place the *S* reflector/Moho approximately 1 km deeper. The depth discrepancy is probably due to the fact that the sediments in the tomographic velocity model are higher on average than in the preferred model, perhaps because the coincident MCS reflection times were not used in the tomographic assessment. The local maximum in Moho depth of 19 km at 125 km model distance is reasonably well matched by both tomographic models, although the maximum is shifted approximately 20 km seaward in the tomographic velocity model and approximately 20 km landward for the tomographic reflection Moho. The local minimum in Moho depth of 16 km at 230 km model distance is well matched by both tomographic models, although the minimum is approximately 2 km shallower in the tomographic velocity model and approximately 2 km deeper and 10 km landward for the tomographic reflection Moho. The thick accumulation of sediments between 215 and 255 km is present in the tomographic velocity model (Fig. 10c), although spread out more laterally and with higher velocities; this is clear in the horizontal slice through the models at 7 km depth (Fig. 9f).

6.4 Chilean margin

The most prominent features of the preferred model from the Chilean margin are: (1) the slope sediments, (2) the Valparaiso forearc basin, (3) the accretionary wedge and (4) the subducting oceanic plate (Fig. 7a). The low-velocity layer representing subducted sediments is the most uncertain and contentious model feature. By comparison with the model for the other dip profile approximately 75 km to the south (Naumenko 2001), features of the preferred model that likely reflect the influence of the subducting Juan Fernández Ridge, and possibly a subducted seamount, include the Valparaiso forearc basin, a velocity decrease in the lower oceanic crust to $\sim$6.7 km s^{-1}, and an increased Moho depth of 1–2 km beneath the accretionary wedge.

The thin layer of slope sediments is present in the tomographic velocity model, but it does not include the sediment thickening in the trench near 60 km model distance as in the preferred model. The Valparaiso basin is clear in the tomographic model and the perturbation plot (Fig. 10d), although its shape is smoothed out as expected; this is apparent in the horizontal slice through the models at 4 km depth (Fig. 9h). The accretionary wedge with velocities in the 3–5 km s^{-1} range is also clear in the tomographic model, although in a smoother form; the close agreement between the two models for this feature is best illustrated by the horizontal slice through the models at 7.5 km depth (Fig. 9h). The subducting oceanic plate is expressed in the tomographic velocity model, although the 7.0–7.6 isovelocity contours representing the oceanic Moho are broken into a shallow portion and a deeper portion with roughly the same slope as the subducting Moho in the preferred model. By comparison, the tomographic reflection Moho agrees closely with the preferred Moho over the full range they are constrained. The most contentious feature of the preferred model is the subducting sediments, represented by a thin low-velocity layer on top of the subducting oceanic plate (Fig. 7a and the horizontal slice at 16 km depth in Fig. 9h). There is no counterpart to this feature in the tomographic velocity model, but this is not surprising given that it is constrained by a few wide-angle reflections off its top and bottom, which were not used in the tomographic inversion. Also, two other subtle features of the preferred model that are interpreted to be related to the subducting Juan Fernández ridge, a slight lowering of oceanic crustal velocities and a thickening of the oceanic crust, both beneath the accretionary wedge, are not apparent in the tomographic velocity model, probably because they are small in magnitude and not required by the first-arrival data.

7 DISCUSSION AND CONCLUSIONS

We have shown that for a wide range of crustal seismic wide-angle data sets and models, the same form of tomographic assessment can be applied in an objective way to establish the most robust features of a preferred model. We intentionally chose four data sets that are quite different in terms of shot–receiver density, the number of refracted and reflected phases, the amount of prior information, the availability of coincident MCS data and the geological setting. The preferred model for each data set was obtained by applying the widely used algorithm of Zelt & Smith (1992), which offers the flexibility to incorporate subjective and prior information to yield what is considered to be the most geologically reasonable model, and therefore, the preferred model. This is one end-member modelling approach advocated by Zelt (1999). The other end-member approach advocated by Zelt (1999) is the usual way in which tomography is applied, that is, with a finely gridded parametrization seeking a smooth or minimum-structure model, using only one or two prominent phases, and little or no prior information. This approach is designed to yield a model that only contains structure required by the most certain data as opposed to structure that is merely consistent with the data. This type of tomography can be applied in perhaps the most objective way possible for a given set of wide-angle traveltime data, i.e. using no prior information and only a few free parameters for which the values, within a somewhat predictable range, do not greatly affect the final model. In this paper we have exploited the minimum-structure and objective characteristics of traditional tomography to carry out the assessment of the preferred models.

This paper has also shown a way in which the modelling/inversion of wide-angle traveltime data can move in the direction of a more transparent and automated approach, as opposed to one that appears to be quite subjective and ad hoc. In particular, our tomographic results have shown that in many cases, particularly data sets with dense shots and receivers, the objective tomographic approach may be sufficient for deriving the 'preferred' model, or at least supplying a model from which the main geological interpretation can be based, since it may contain all of the structure

Downloaded from https://academic.oup.com/gji/article/153/3/609/671989 by U.S. Department of Justice user on 16 August 2022

of interest. This assertion is based on the amount of structure we see in the smooth, tomographically derived models that is consistent with the more subjectively derived preferred models. Even for relatively sparsely sampled data, such as the Canadian Cordillera data, tomographic assessment appears to be worthwhile since the smooth model can contain significant structure. If the tomographic approach is not entirely sufficient, for example, if it is not able to exploit all the prior information and wide-angle data, and possibly pre-conceived notions of what is geologically reasonable, we have tried to show that it is reasonable to use a more subjective approach to develop the preferred model, particularly if it is coupled with the type of tomographic assessment presented here. The tomographic model is not intended to supersede the preferred model, since the latter model is typically better resolved and more interpretable. Tomographic assessment is intended to lend credibility to model features common to the tomographic and preferred models.

If the tomographic approach is used to derive the preferred model, it can also be used for model assessment by thoroughly exploring model space using a range of free parameter values, including the starting model, and by using subsets of the complete data set which omit phases or picks that are more difficult to identify than others. For the purpose of this paper, a range of free parameters was not explored in order to emphasize that the tomographic approach can be carried out in a nearly automated and non-subjective fashion, regardless of the data set or model type. In practice, one should vary the free parameters in a systematic way to understand their effect on the final model. Our experience with the data sets in this paper and others suggests that the tomographic results are not highly sensitive to the values of the free parameters discussed earlier in this paper.

Despite the general consistency between the preferred and tomographic models for the four data sets in this paper, significant differences also exist as described in the previous section. However, these differences are generally within the uncertainties typically assigned to crustal velocity models obtained from wide-angle data; for example, ± 2 km for Moho depth. There are also differences due to the fact that the tomographic models are smooth and the preferred models consist of multiple layers, some with velocity discontinuities between them. The layer boundaries in the preferred models may give the illusion of higher spatial resolution, or 'sharpness', but this is an artefact arising from the convenience of using discontinuities to model reflections when ray-trace modelling. In fact, observed reflections could be generated by relatively thick zones with a simple gradient or complex internal structure. Nevertheless, because of the smooth, non-layered model parametrization used in the refraction tomography, the tomographic velocity model is best used as a check on the long-wavelength structure and relative velocity variations in the preferred model, as opposed to the velocity at a specific point (Fig. 9). The Canadian and Chilean tomographic models appear to show the least agreement with the corresponding preferred model, at least with respect to features that were deemed geologically significant in the preferred models. For the Canadian data this is likely because it is the most sparsely sampled. For the Chilean data this is likely because many of the preferred model features were derived using reflections and introducing many layers, aspects not involved in the refraction tomography approach.

As described earlier, the more subjective approach we have used to derive the preferred models and the tomographic approach we have used for model assessment represent two end-member modelling styles. Their extreme differences make them well suited to complement one another, in that the former can be used to explore the limits of what model structure is consistent with the wide-angle data, and the latter can be used to isolate what model structure is required by the wide-angle data. Although we believe these two methods may be the best pair to apply in most cases, intermediate or hybrid modelling approaches will likely prove useful in some cases.

By demonstrating the effectiveness of tomographic assessment, this paper has addressed several related issues, such as: (1) the robustness of first-arrival and reflection tomography, even for relatively sparsely sampled data and even in the presence of large 2-D velocity perturbations (Fig. 10), (2) it is the more subjective modelling steps that provide, or give the impression of providing, the higher resolution or 'sharpness' in the preferred models that does not appear in the tomographic velocity models, (3) a set of guidelines for interpreting smooth tomographic velocity models based on the ground truth provided by a set of real case studies and (4) wide-angle survey design, in the sense that the four case studies in this paper demonstrate the possibilities and limitations of typical data sets to image a range of geological structures.

ACKNOWLEDGMENTS

The acquisition of the four data sets was funded by Lithoprobe (Canada), the CSS project of the National Geophysical Research Institute of India, the National Science Foundation (USA) and the German Ministry for Science and Technology. KS acknowledges the financial assistance from the Ministry of Science and Technology, New Delhi, India for the BOYSCAST (postdoctoral) Fellowship to work at Rice University. A review of an earlier version of the paper by B. Zelt is gratefully acknowledged.

REFERENCES

Ahmed, F., 1964. The line of Narmada-Son valley, *Curr. Sci.,* **33,** 362–363.

Choubey, V.D., 1971. Narmada-Son lineament, India, *Nat. Phys. Sci.,* **232,** 38–40.

Clowes, R.M., Zelt, C.A., Amor, J.R. & Ellis, R.M., 1995. Lithospheric structure in the southern Canadian Cordillera from a network of seismic refraction lines, *Can. J. Earth Sci.,* **32,** 1485–1513.

Comte, D., Roecker, S.W. & Suarez, G., 1994. Velocity structure in northern Chile: evidence of subducted oceanic crust in the Nazca Plate, *Geophys. J. Int.,* **117,** 625–639.

Flueh, E.R. *et al.*, 1998. Seismic investigation of the continental margin off and onshore Valparaiso, Chile, *Tectonophysics,* **288,** 251–263.

Ghosh, D.B., 1976. The nature of Narmada-Son lineament, in *Seminar volume on Tectonics and Metallurgy of South and East Asia,*, *Geol. Surv. India, Misc. Publ.,* **34,** 119–132.

Hole, J.A. & Zelt, B.C., 1995. Three-dimensional finite-difference reflection travel times, *Geophys. J. Int.,* **121,** 427–434.

Kaila, K.L., Murty, P.R.K., Mall, D.M., Dixit, M.M. & Sarkar, D., 1987. Deep seismic soundings along Hirapur-Mandla profile, central India, *Geophys. J. R. astr. Soc.,* **89,** 399–404.

Kaila, K.L., Murty, P.R.K. & Mall, D.M., 1989. The evolution of the Vindhyan basin vis-à-vis the Narmada-Son lineament, central India, from deep seismic soundings, *Tectonophysics,* **162,** 277–289.

Korenaga, J., Holbrook, W.S., Kent, G.M., Kelemen, P.B., Detrick, R.S., Larsen, H.-C., Hopper, J.R. & Dahl-Jensen, T., 2000. Crustal structure of the southeast Greenland margin from joint refraction and reflection seismic tomography, *J. geophys. Res.,* **105,** 21 591–21 614.

Lees, J.M. & Crosson, R.S., 1989. Tomographic inversion for three-dimensional velocity structure at Mount St Helens using earthquake data, *J. geophys. Res.,* **94,** 5716–5728.

Levander, A.R. & Holliger, K., 1992. Small-scale heterogeneity and large-scale velocity structure of the continental crust, *J. geophys. Res.,* **97,** 8797–8804.

Downloaded from https://academic.oup.com/gji/article/153/3/609/671989 by U.S. Department of Justice user on 16 August 2022

Lutter, W.J., Fuis, G.S., Thurber, C.H. & Murphy, J., 1999. Tomographic images of the upper crust from the Los Angeles Basin to the Mojave Desert, California: Results from the Los Angeles Region Seismic Experiment, *J. geophys. Res.,* **104,** 25 543–25 565.

McCaughey, M. & Singh, S.C., 1997. Simultaneous velocity and interface tomography of normal-incidence and wide-aperture traveltime data, *Geophys. J. Int.,* **131,** 87–99.

Naumenko, J.V., 2001. Seismic traveltime inversion of wide-angle data for strongly-varying structure: central Chilean margin and the subducting Juan Fernandez Ridge, *MA thesis*, Rice University.

Nolet, G., 1987. Seismic wave propagation and seismic tomography, in, *Seismic Tomography,* ed. Nolet, G., pp. 1–24, Reidel, Dordecht.

Sain, K., Bruguier, N., Murty, A.S.N. & Reddy, P.R., 2000. Shallow structure along the Hirapur-Mandla profile using traveltime inversion of wide-angle seismic data, and its tectonic implications, *Geophys. J. Int.,* **142 ,** 505–515.

Sawyer, D.S., Zelt, C.A. & Reston, T., 1998. Imaging above and below the, *S* reflector, Galicia Bank Basin: MCS and OBS results, *EOS, Trans. Am. geophys. Un.,* **79,** F652.

Scales, J.A., Docherty, P. & Gersztenkorn, A., 1990. Regularisation of nonlinear inverse problems: imaging the near-surface weathering layer, *Inverse Problems,* **6,** 115–131.

Tichelaar, B.W. & Ruff, L.J., 1991. Seismic coupling along the Chilean subduction zone, *J. geophys. Res.,* **96,** 11 997–12 022.

Unger, M.R., 2001. Structural and tectonic interpretation of deep seismic reflection data offshore Spain and Portugal: a tectonic rifting model, *MA thesis*, Rice University.

Vidale, J.E., 1988. Finite-difference calculation of traveltimes, *Bull. seism. Soc. Am.,* **78,** 2062–2076.

von Huene, R., Corvalan, J., Flueh, E.R., Hinz, K., Korstgard, J., Ranero, C.R., Weinrebe, W. & the CONDOR Scientists, 1997. Tectonic control of the subducting Juan Fernandez Ridge on the Andean margin near Valparaiso, Chile, *Tectonics,* **16,** 474–488.

West, W.D., 1962. The line of Narmada-son valley, *Curr. Sci.,* **31,** 143–144.

White, D.J. & Boland, A.V., 1992. A comparison of forward modeling and inversion of seismic first arrivals over the Kapuskasing Uplift, *Bull. seism. Soc. Am.,* **82,** 304–322.

Zelt, C.A., 1994. 3-D velocity structure from simultaneous traveltime inversion of in-line seismic data along intersecting profiles, *Geophys. J. Int.,* **118,** 795–801.

Zelt, C.A., 1999. Modeling strategies and model assessment for wide-angle seismic traveltime data, *Geophys. J. Int.,* **139,** 183–204.

Zelt, C.A. & Barton, P.J., 1998. Three-dimensional seismic refraction tomography: a comparison of two methods applied to data from the Faeroe Basin, *J. geophys. Res.,* **103,** 7187–7210.

Zelt, C.A. & Smith, R.B., 1992. Seismic traveltime inversion for 2-D crustal velocity structure, *Geophys. J. Int.,* **108,** 16–34.

Zelt, C.A. & White, D.J., 1995. Crustal structure and tectonics of the southeastern Canadian Cordillera, *J. geophys. Res.,* **100,** 24 255–24 273.

Zelt, C.A., Hojka, A.M., Flueh, E.R. & McIntosh, K.D., 1999. 3D simultaneous seismic refraction and reflection tomography of wide-angle data from the central Chilean margin, *Geophys. Res. Lett.,* **26,** 2577–2580.

Zelt, C.A., Sawyer, D.S., Nakamura, Y. & Reston, T.J., 2003. Crustal structure of the iberia margin at 42°N from simultaneous inversion of seismic wide-angle and zero-offset traveltime data, *Geophys. J. Int.,* submitted.

Downloaded from https://academic.oup.com/gji/article/153/3/609/671989 by U.S. Department of Justice user on 16 August 2022